doi: 10.1111/j.1751-3928.2008.00049.x *Resource Geology* Vol. 58, No. 2: 124–142

Original Article

Magmatic evolution of the Mantos Blancos copper deposit, Coastal Range of northern Chile: insight from Sr–Nd isotope, geochemical data and silicate melt inclusions

Luis E. Ramírez[1], Miguel A. Parada[1], Carlos Palacios[1] and Jens Wittenbrink[2]

[1]*Department of Geology, University of Chile, Santiago, Chile* [2]*Institute of Minerology and Mineral Resources, Technical University of Clausthal, Clausthal-Zellerfeld, Germany*

Abstract

The Mantos Blancos copper deposit (500 Mt at 1.0% Cu) was affected by two superimposed hydrothermal events: (i) phyllic alteration related to a rhyolitic dome emplacement and brecciation at *ca* 155 Ma; and (ii) potassic, sodic and propylitic alteration at *ca* 142 Ma, coeval with stocks and sills emplacement of dioritic and granodioritic porphyries, that locally grade upwards into polymictic magmatic hydrothermal breccias. Major hypogene copper sulfide mineralization is related to the second event. A late-ore mafic dike swarm cross-cuts all rocks in the deposit. Two types of granodioritic porphyries can be distinguished from petrographic observations and geochemical data: granodiorite porphyry I (GP I) and granodiorite porphyry II (GP II), which resulted from two different trends of magmatic evolution. The concave shape of the rare earth element (REE) distribution pattern together with the weak or absence of negative Eu anomalies in mafic dikes, dioritic and GP I porphyries, suggest hornblende-dominated fractionation for this magmatic suite. In contrast, distinct negative Eu anomalies and the flat REE patterns suggest plagioclase-dominated fractionation, at low oxygen fugacity, for the GP II porphyry suite. But shallow mixing and mingling between silicic and dioritic melts are also likely for the formation of the GP II and polymictic breccias, respectively. Sr-Nd isotopic compositions suggest that the rhyolitic dome rocks were generated from a dominantly crustal source, while the GP I has mantle affinity. The composition of melt inclusions (MI) in quartz crystals from the rhyolitic dome is similar to the bulk composition of their host rock. The MI analyzed in quartz from GP II and in the polymictic magmatic hydrothermal breccia of the deposit are compositionally more evolved than their host rocks. Field, geochemical and petrographic data provided here point to dioritic and siliceous melt interaction as an inducing mechanism for the release of hydrothermal fluids to form the Cu mineralization.

Keywords: Chile, coastal range, cu mineralization, Sr-Nd isotopes, magma mixing.

1. Introduction

The Coastal Range of northern Chile hosts numerous copper deposits, constituting a NS-trending Late Jurassic–Early Cretaceous metallogenic belt, which extends for more than 200 km (22°–24°S; Fig. 1). Two main types of ore deposits occur in this copper province: volcanic-hosted strata-bound orebodies (Espinoza *et al.*, 1996; Maksaev & Zentilli, 2002) and porphyry copper deposits (Camus, 2003). Other ore deposits are hosted in intrusive rocks and were described by Espinoza *et al.* (1996) as vein type deposits.

Received 11 July 2006. Accepted for publication 26 August 2007.
Corresponding author: L. E. RAMÍREZ, Departamento de Geología, Universidad de Chile, PO Box 13518-21, Santiago, Chile.
Email: lramirez@cec.uchile.cl

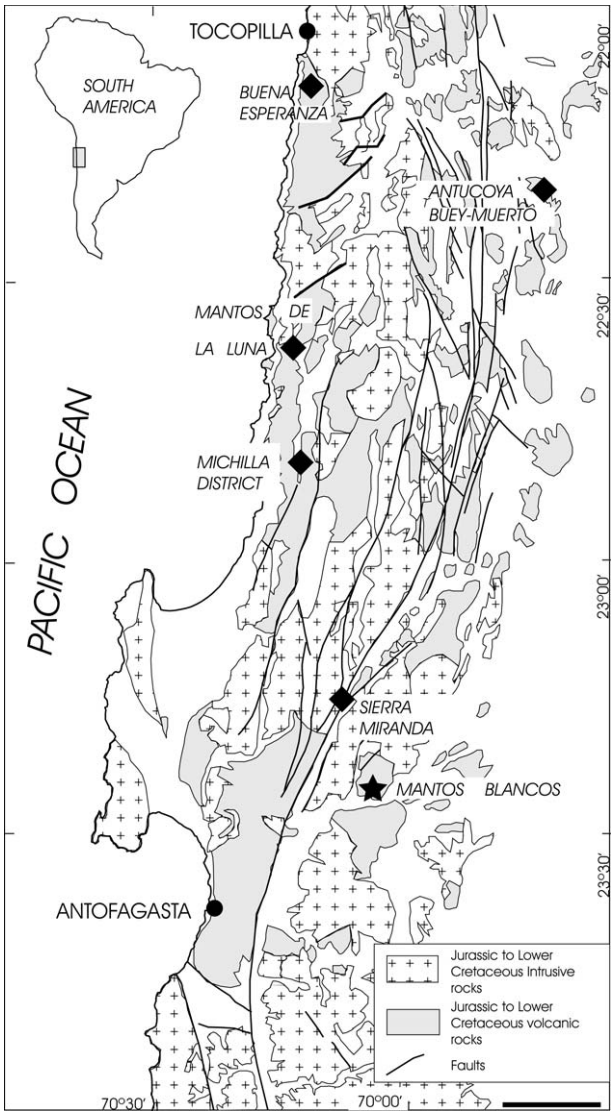

Fig. 1 Geological map of the Coastal Cordillera, Northern Chile, and location of the Mantos Blancos ore deposit (★) and other Late Jurassic Early Cretaceous volcanic-hosted copper deposits (◆). Modified after Maksaev and Zentilli (2002). Bar, 20 km.

The volcanic-hosted strata-bound ore deposits are characterized by magmatic and hydrothermal breccias that form feeder structures to the flat-lying peripheral stratiform mineralization. The hydrothermal breccias contain a major portion of the commercial mineralization and have the highest ore grade in these deposits. The pipes-like hydrothermal breccias are genetically related to coeval stocks and sills of mainly dioritic composition, and are intruded by post-mineralization basaltic dikes (Maksaev & Zentilli, 2002). The porphyry copper mineralization in the belt is associated with granodioritic porphyries and hydrothermal breccias (Perelló *et al.*, 2003). The Mantos Blancos deposit produces approximately 50% of all copper of the belt, and had pre-mining resources of 500 million tons with 1.0% Cu (Ramírez *et al.*, 2006). The ore deposit was formed by two main hydrothermal events: (i) a first event (*ca* 155 Ma) related to rhyolitic magmatism and magmatic hydrothermal monomictic breccias of rhyolitic composition; and (ii) a second event (*ca* 142 Ma) related to dioritic and granodioritic porphyries and magmatic hydrothermal polymictic breccias (Ramírez *et al.*, 2006). We here present new geochemical, isotopic and silicate melt inclusion (MI) data of the Mantos Blancos district, in order to better understand its magmatic evolution. Additionally, the role of the magmatic processes in the associated hydrothermal alteration is discussed.

2. Geological setting

During the Jurassic–Early Cretaceous a subduction-related magmatic belt developed along the present Coastal Range of northern Chile. It is represented by 7000-m-thick basaltic–andesitic volcanic pile (La Negra Formation) and granitic–dioritic plutonic rocks. The volcanic sequence has mantle affinity (Rogers & Hawkesworth, 1989; Lucassen *et al.*, 2002) and evolved with time from an initial stage of tholeiitic affinity to calc-alkaline composition (Palacios, 1984; Rogers & Hawkesworth, 1989; Pichowiak *et al.*, 1990; Kramer *et al.*, 2005). Three main plutonic events have been described in the Coastal Range of northern Chile (Andriessen & Reutter, 1994; Pichowiak, 1994; Scheuber, 1994; Dallmeyer *et al.*, 1996; Scheuber & González, 1999): Early Jurassic (200–180 Ma) granitic–tonalitic rocks, Middle Jurassic (170–160 Ma) granodioritic rocks, and Late Jurassic–Early Cetaceous (155–140 Ma) granodioritic–dioritic rocks. The tectonic evolution of the Coastal Range during the Jurassic is interpreted in terms of coupling and decoupling between the down-going and overriding plates, in a transtensional regime due to oblique subduction (Scheuber & Gonzalez, 1999). Between 200 and 155 Ma an intra-magmatic belt, controlled by the NS-trending sinistral strike–slip Atacama Fault Zone was developed. But at the end of the Jurassic, and due to foundering of the subducting plate, subduction rollback and decoupling, the emplacement of the magmatic belt was controlled by an EW-trending extensional regime (Scheuber & Gonzalez, 1999).

3. Geology of the deposit

The lithological units recognized within the Mantos Blancos ore deposit consist of a rhyolitic dome and magmatic hydrothermal monomictic breccias of the same composition, intruded by stocks and sills of dioritic and granodioritic porphyries. The dioritic and granodioritic stocks locally grade upwards into magmatic hydrothermal polymictic breccias. These rock units are all mineralized to a variable degree. Late mafic dike swarms cross-cut all previously mentioned rock units and are essentially barren (Ramírez *et al.*, 2006; Fig. 2).

3.1. Rhyolitic dome and associated magmatic hydrothermal rhyolitic breccias

The dome structure has been identified by the restoration of its pre-mining geometry by studying drill core logs of the early stage of exploitation (Chávez, 1985). Drill cores located in the vicinity of the mine also provide evidence of an outward decreasing thickness, compatible with a dome structure, from the main rhyolitic body of the pit. The rhyolitic dome occupies the most important parts of the deposit, and it is hosted by felsic tuffs and mafic–intermediate lava flows of the La Negra Formation and intruded by stocks and sills of dioritic and granodioritic porphyries. The rhyolitic dome is exposed over 350 m in depth along the walls of the current open pit, but information from drill cores indicates a vertical extent to at least 800 m. Due to pervasive alteration, the contacts between internal flows are very difficult to observe, but near-horizontal and vertical flow laminations of 1–4 cm thickness are recognized. The rhyolitic dome consists of rhyolitic porphyry with 30–60% of feldspar and corroded quartz phenocrysts (1–5 mm) in a highly altered felsic groundmass. Magnetite and zircon are common accessory minerals. Subvertical bodies of magmatic hydrothermal breccia hosted in the rhyolitic dome have been recognized. They are matrix-supported monomictic (rhyolite) breccias approximately 100–250 m in vertical view, and with subcircular horizontal sections of 50–100 m in diameter. The matrix is composed of rhyolitic rock flour with intense alteration and disseminated sulfides. The rhyolitic fragments are altered, irregular in shape, poorly sorted and vary in size between 1 cm and several meters. Although the age of the rhyolitic dome is not known, the age of the hydrothermal event affecting the dome is *ca* 155 Ma ($^{40}Ar/^{39}Ar$ in sericite; Oliveros, 2005) and is probably close to the dome emplacement age.

3.2. Granodioritic and dioritic porphyries, and associated magmatic hydrothermal polymictic breccias

3.2.1. Granodiorite porphyries

Two granodioritic porphyries have been recognized: granodiorite porphyry I (GP I) and granodiorite porphyry II (GP II). Rocks of the GP I are mainly located west and south of the pit, but are also recognized from drill cores in the mine. Commonly it contains 35–50% of 0.5–5-mm large phenocrysts of hornblende, oscillatory-zoned plagioclase and biotite, in a groundmass of quartz, feldspars and minor biotite. GP II is restricted to the ore deposit domain. It contains 10–30% of phenocrysts of 0.5–3 mm large plagioclase (albitized), embayed β-quartz and chloritized hornblende in a groundmass of quartz, feldspars and hematite intergrowth (Fig. 3e, f). Minor amounts of magnetite and zircon have been observed in both GP I and GP II.

3.2.2. Diorite porphyry

The diorite porphyry has 5–10% of 2–5-mm large phenocrysts of pyroxene (and minor hornblende) in a groundmass of fine-grained pyroxene, plagioclase and magnetite. The diorite porphyry exhibits mm-sized spherical miarolitic cavities with quartz and sulfide infill (Fig. 3a) and chlorite sulfide infill (Fig. 3b). Mutual intrusive relationships between both GP II and diorite porphyries are common (Ramírez *et al.*, 2006), and meter–centimeter enclaves of one in the other have been frequently observed (Fig. 3g, h). Recent $^{40}Ar/^{39}Ar$ data on amphibole give ages of 142.2 ± 1 Ma for GP I, and 141.4 ± 0.5 Ma for the diorite porphyry (Oliveros, 2005). Although the age of GP II is not known, the mutual intrusive relationships with the dioritic porphyry suggest that both are coeval.

3.2.3. Polymictic magmatic hydrothermal breccias

Two polymictic and matrix-supported pipe-like magmatic hydrothermal breccias are recognized in the pit of the mine. They are spatially related with N-S faults and hosted within the rhyolitic dome. The largest breccia body, located in the central part of the pit, is cross-cut by metric-sized sills of dioritic porphyry and GP I. The breccias form near-vertical bodies, with a vertical extent of approximately 700 m, and have sub-spherical sections with diameters between 100 and 500 m. The upper part of the breccia pipes exhibits hydrothermal characteristics as evidenced by the presence of a matrix composed of hydrothermal and ore minerals (Fig. 3c, d). The breccia

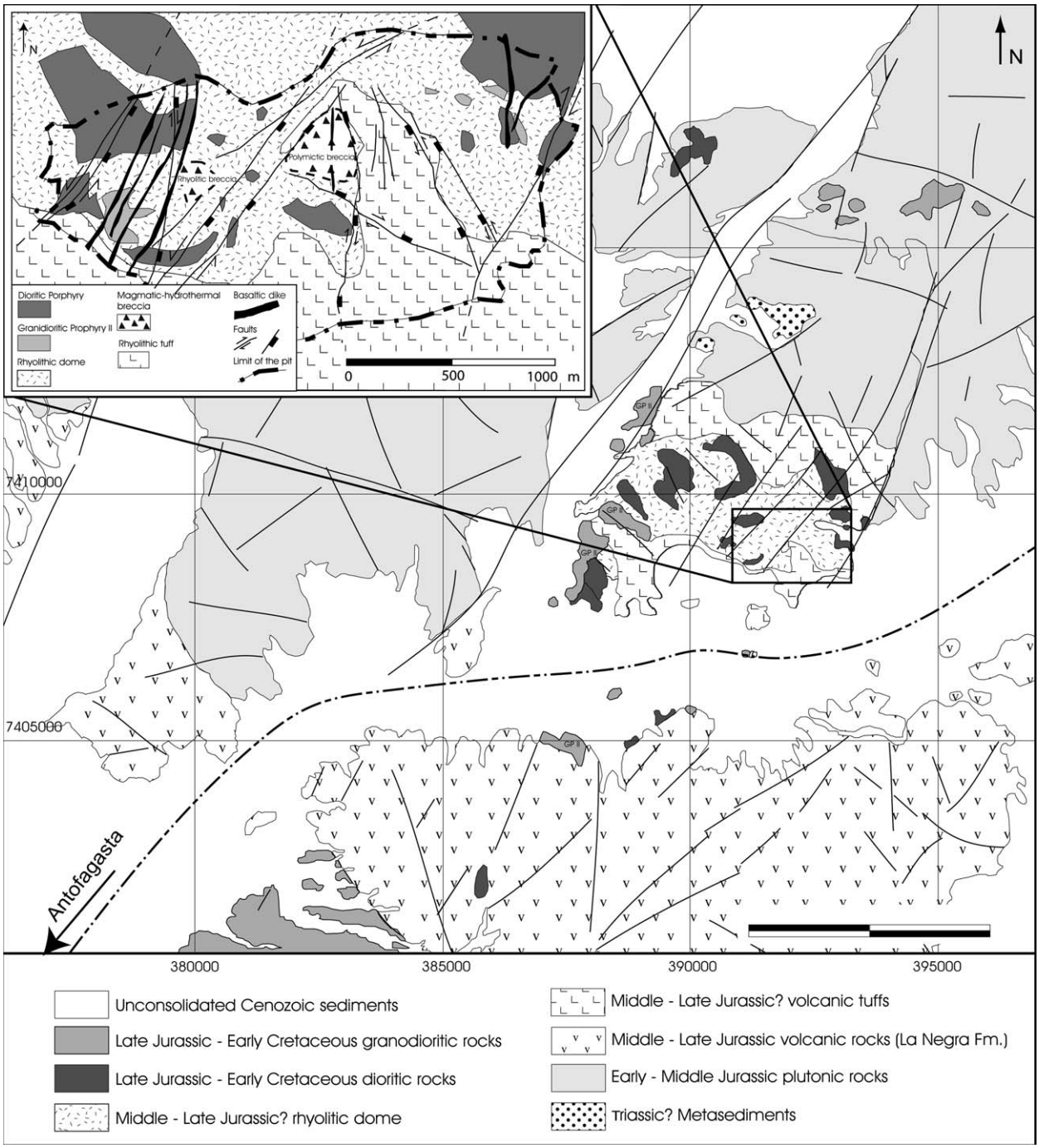

Fig. 2 Geological map of the Mantos Blancos ore deposit. Bar, 5 km.

fragments include angular and sub-rounded altered rocks of the rhyolitic dome and of granodioritic and dioritic porphyries. They are poorly sorted and range in size from 1 cm to 15 m. Downwards in the breccia bodies, magmatic features are progressively more evident. It is common to observe magma mingling as evidenced

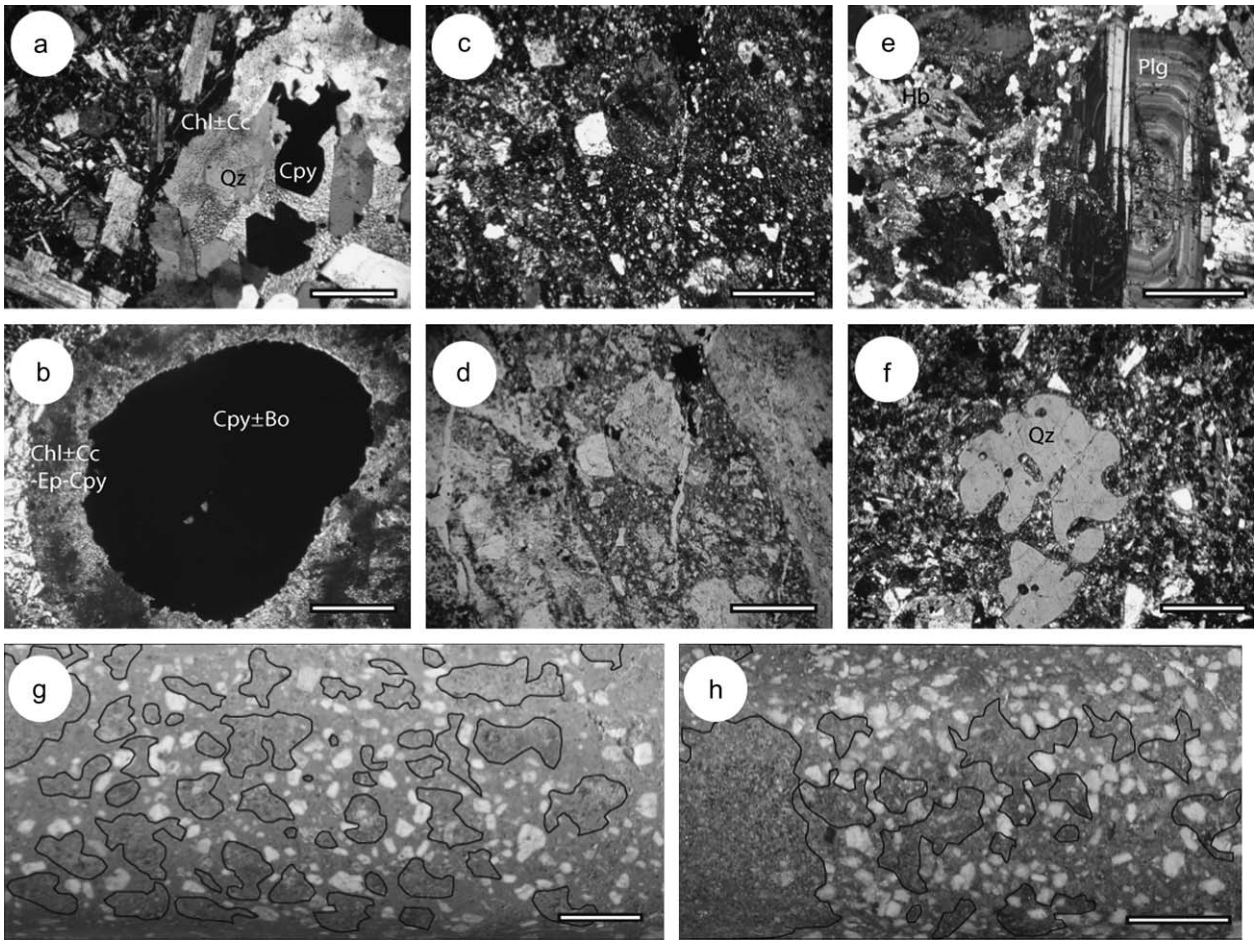

Fig. 3 Microphotographs of different rock units in the Mantos Blancos district. (a) Miarolitic cavity with quartz and sulfide (Cpy) infill in diorite porphyry (cross-polarized light, sample CPM-1-2); (b) miarolitic cavity with sulfide (Cpy ± Bo) infill with a border zone of chlorite, calcite, epidote and chalcopyrite in diorite porphyry (cross-polarized light, sample CPM-1-15); (c) mineralized polymictic magmatic hydrothermal breccia with cross-polarized light; and (d) with plane-polarized light (sample P-4-1); (e) oscillatory-zoned plagioclase phenocryst in granodiorite porphyry I (GP I; cross-polarized light, sample MB-2-3); (f) reabsorbed quartz phenocryst in GP II (cross-polarized light, sample 11497-320); (g, h) Pictures of dioritic micro-enclaves in GP II. Bars: a–f, 1 mm; g, h, 1 cm. Bo, bornite; Cc, calcite; Chl, chlorite; Cpy, chalcopyrite; Ep, epidote; Plg, plagioclase; Qz, quartz.

by granodioritic enclaves in a dioritic matrix, as well as dioritic enclaves in a granodioritic matrix (Fig. 3g, h).

3.3. Mafic dike swarm

Most mafic dikes are subvertical oriented in NNE direction, although NS and NNW subvertical dikes also occur. The dikes are 1–12 m thick and represent approximately 15% of the total rock volume in the deposit. They exhibit porphyritic texture, with 10–25% of 3–10-mm altered plagioclase, hornblende and minor pyroxene phenocrysts, in a very fine-grained groundmass of feldspar, hornblende, and subordinately biotite and magnetite. A hornblende $^{40}Ar/^{39}Ar$ age of 142.7 ± 2.1 Ma was obtained for a weak late-mineralized dike in the mine (Oliveros, 2005).

3.4. Hydrothermal alteration and mineralization

The deposit was affected by two overprinted hydrothermal events: (i) a phyllic alteration event related to the rhyolitic dome emplacement and rhyolitic magmatic hydrothermal brecciation that took place at *ca* 155 Ma; and (ii) a potassic-propylitic-sodic alteration event that developed at *ca* 141–142 Ma, coeval with the

stocks and sills intrusion of dioritic and granodioritic porphyries. This second hydrothermal event is related to the main mineralization pulse, which occurs disseminated and in stockworks centered in the polymictic magmatic hydrothermal breccias (Ramírez *et al.*, 2006). Hypogene sulfide assemblages have a vertical and lateral zoning within polymictic breccia bodies. A barren pyrite root zone is overlain by pyrite–chalcopyrite, and followed upwards and laterally by chalcopyrite–digenite or chalcopyrite–bornite. The assemblage digenite–supergene chalcocite characterizes the central portions of high-grade mineralization in the polymictic breccia bodies (Ramírez *et al.*, 2006).

4. Whole rock geochemistry

Major oxide, trace, and rare earth element (REE) contents of 52 representative samples from the Mantos Blancos ore deposit are listed in Table 1. Geochemical analyses were carried out using inductively coupled plasma atomic emission spectometer (ICP-AES) (Perkin Elmer P-430) at the Department of Geology, University of Chile. The USGS standards BCR-2, AGV-2 and G-2 were used for calibration. Because of the widespread hydrothermal alteration, the rock classification is by immobile elements according to the Floyd and Winchester (1978) diagram for volcanic rocks. Figure 4

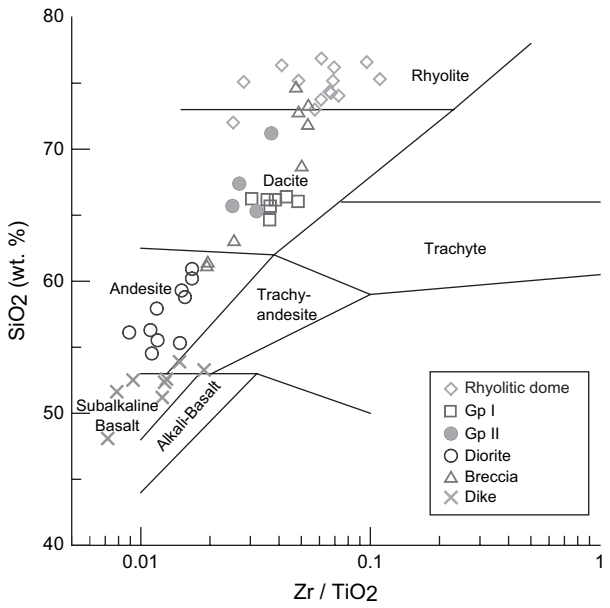

Fig. 4 Immobile element classification of major rock units of the Mantos Blancos deposit. After Floyd and Winchester (1978).

indicates that samples of the dioritic and granodioritic porphyries fall in the fields of its volcanic counterparts (andesite and dacite), respectively. Most rocks of the felsic dome are rhyolitic in composition and rocks of the mafic dike swarm plot in the basaltic field. The REE chondrite-normalized patterns for different rock units are shown in Figure 5. The rhyolite samples show strongly fractionated light rare earth elements (LREE) patterns with distinct negative Eu anomalies and flat heavy rare earth elements (HREE) patterns. The GP I samples have concave REE patterns and no Eu anomaly. The GP II samples differ from the GP I samples in their negative Eu anomalies and in the less fractionated HREE patterns. The rocks of the dioritic porphyries and late-ore basaltic dikes exhibit similar gently dipping slightly fractionated REE patterns with a small Eu depletion.

5. Sr-Nd isotopes and the nature of the magma sources

The analyzed samples of Mantos Blancos district (Table 2) have different isotopic signatures. The analytical isotope procedure is presented in Appendix I. Two samples from GP I have initial $^{87}Sr/^{86}Sr$ ratios of 0.70362 and 0.70395 and εNd values of +3.5 and +3.2, respectively. These data suggest a dominant mantle source and are similar to the reference data for La Negra Formation (Rogers & Hawkesworth, 1989; Lucassen *et al.*, 2002; Fig. 6). The rhyolitic dome has an initial $^{87}Sr/^{86}Sr$ ratio of 0.70592 and an εNd value of −2.0, suggesting more crustal involvement. A sample from the igneous matrix of the Mantos Blancos polymictic breccia has an initial $^{87}Sr/^{86}Sr$ ratio of 0.70591, similar to that of the rhyolitic dome, and an εNd of +0.15, suggesting a mixed source between the rhyolitic dome and the GP I. Three samples of the dioritic porphyry (F. Munizaga, pers. comm., 2006) from the open pit have intermediate isotopic composition between the GP I porphyry (included in the field of volcanic rocks of the La Negra Formation) and the rhyolitic dome ($^{87}Sr/^{86}Sr$ initial ratios range between 0.70455 and 0.70573 and εNd values between 0.0 and +2.5; Fig. 6). No isotope data exist for the basaltic dikes of the deposit, but because of the chemical compositional similarities between the basaltic dikes and mafic lavas of the La Negra Formation (Rogers & Hawkesworth, 1989; Lucassen *et al.*, 2002) and Cretaceous dikes in the region (Lucassen *et al.*, 2002), a depleted isotopic signature is assumed for the Mantos Blancos dikes.

Table 1 Whole rock analyses from Mantos Blancos magmatic rocks Major elements in wt%, trace elements in ppm

	Rhyolitic dome														
Sample	CPM-1.1	CPM-1.12	CPM-1.16	CPM-1.17	CPM-1.18	CPM-1.20	CPM-1.24	CPM-1.28	CPM-1.4	CPM-1.6	CPM-1.8	CPM-1.9	MB-2.6	MB1‡	MB5‡
Wt%															
SiO^2	75.19	76.36	72.02	74.27	74.35	76.60	76.87	76.20	75.31	79.00	74.05	75.10	75.18	73.76	74
TiO^2	0.22	0.28	0.57	0.19	0.19	0.11	0.17	0.18	0.14	0.40	0.15	0.41	0.15	0.36	0.19
Al^2O^3	13.75	11.92	14.42	15.26	14.66	13.81	12.64	13.02	14.13	12.80	15.02	13.02	11.94	14.23	13.6
Fe^2O^3	0.45	1.58	1.35	0.23	<0.1	0.37	0.20	0.74	<0.1	1.44	0.34	0.25	1.64	1.25	1.67
FeO	0.12	0.20	0.08	<0.1	<0.1	0.08	0.96	0.08	<0.1	0.88	<0.1	<0.1	1.08	—	—
MnO	0.01	0.01	0.01	0.01	0.01	0.01	0.01	0.01	0.01	0.01	0.01	0.01	0.04	0.01	0.02
MgO	0.18	0.32	0.14	0.01	0.05	0.01	0.65	0.07	0.02	0.82	0.10	0.02	1.22	0.08	0.04
CaO	0.02	0.01	1.02	0.40	0.45	0.20	0.09	0.11	0.75	0.24	0.21	1.38	0.01	0.08	0.58
Na^2O	4.46	2.50	7.62	8.50	8.57	7.68	6.94	7.60	8.40	7.31	8.82	8.07	5.38	7.65	7.87
K^2O	3.76	4.62	0.12	0.04	0.46	0.03	0.03	0.08	0.08	0.06	0.05	0.02	1.48	0.04	0.13
P^2O^5	0.01	0.04	0.07	0.06	0.04	N/D	0.04	0.05	0.02	N/D	0.03	0.08	0.06	0.08	0.07
LOI %	1.61	1.86	2.36	0.60	0.79	0.57	0.95	0.99	0.80	1.98	0.82	1.40	1.40	1.80	1.54
Total	99.78	99.70	99.78	99.57	99.57	99.47	99.55	99.73	99.66	98.94	99.60	99.76	99.58	99.34	99.7
PPM															
Ba	475	654	23	22	43	21	21	22	26	21	25	17	126	8	12
Sr	85	106	54	41	39	27	36	80	27	39	60	28	47	39	36
Nb	5.6	5.6	5.6	5.0	5.0	5.0	3.8	4.4	3.8	5.6	4.4	5.6	3.8	6.0	7
Hf	2.5	4.6	4.8	3.7	3.5	3.7	2.4	2.7	4.2	6.4	3.6	3.6	1.3	5.1	2.8
Zr	107	115	144	128	126	106	104	125	154	229	109	115	103	222	129
Y	9	23	18	14	19	22	9	16	21	32	12	23	14	29	26
Th	13.0	12.0	10.0	13.0	15.0	9.3	11.0	11.0	12.0	14.0	13.0	13.0	13.0	11.6	9.4
Cr	21	34	23	16	15	20	18	19	12	21	25	17	13	<1	<1
Co	3	6	6	4	3	2	4	2	2	4	4	3	6	1	2
Sc	4	6	6	3	3	4	2	4	5	7	2	5	3	5	5
V	28	24	38	12	11	6	18	12	18	27	7	13	16	25	11
Cu	96	485	470	880	66	1540	29	730	35	5700	155	83	920	1103	2185
Zn	3	2	8	2	2	3	52	2	2	53	3	6	40	11	14
Ni	4	6	6	2	6	4	2	2	3	2	1	2	5	7	2
La	9	16	15	12	10	5	9	17	5	15	7	7	8	12	8.2
Ce	21	40	34	23	24	13	17	35	14	36	18	21	18	25	18
Nd	10	21	17	13	13	9	10	16	8	20	7	12	12	11	8
Sm	2.04	4.45	3.28	2.43	2.69	2.26	1.54	2.59	1.88	3.91	1.40	2.37	1.92	3.80	2.9
Eu	0.25	0.53	0.74	0.43	0.40	0.27	0.27	0.44	0.35	0.78	0.32	0.45	0.45	0.60	0.4
Gd	2.10	3.94	3.64	2.47	3.17	3.05	1.65	2.46	2.57	5.22	1.84	3.21	2.40	—	—
Dy	2.30	4.22	3.54	2.82	3.69	3.80	1.92	3.01	3.03	6.12	2.28	3.98	2.45	—	—
Ho	0.48	0.93	0.72	0.63	0.78	0.84	0.42	0.68	0.63	1.30	0.50	0.88	0.50	—	—
Er	1.42	2.64	2.01	1.81	2.13	2.46	1.18	1.96	1.81	3.60	1.45	2.58	1.40	—	—
Yb	1.36	2.51	2.05	1.80	2.12	2.42	1.16	1.93	1.85	3.65	1.41	2.50	1.41	2.70	2
Lu	0.22	0.40	0.33	0.29	0.32	0.37	0.18	0.30	0.30	0.58	0.23	0.40	0.21	0.41	0.3
TempZr (°C)	760	775	755	761	750	753	753	764	765	803	743	724	753	812	750

continued

Table 1 Continued

	GP I					GP II						Diorite porphyry		
Sample	MB-2.1	MB-2.3	MB-2.7	MB-2.8	1301–208†	MB3‡	MB4‡	CPM-1.14a	1301–350†	1301–363†	11497–320†	CPM-1.11	CPM-1.15	CPM-1.2
Wt														
SiO^2	66.17	66.05	65.69	66.18	66.25	64.66	66.40	71.20	67.39	65.70	65.30	59.30	56.12	54.53
TiO^2	0.35	0.38	0.44	0.40	0.49	0.46	0.40	0.47	0.82	0.87	0.73	1.07	1.45	1.45
Al^2O^3	15.88	16.47	15.43	16.48	15.59	15.77	15.53	12.71	14.40	14.25	16.57	16.73	19.07	19.16
Fe^2O^3	2.02	1.60	2.14	1.82	1.26	3.88	3.42	0.93	2.25	3.58	1.09	1.23	2.15	3.24
FeO	1.36	1.72	1.64	1.60	3.24	—	—	3.32	2.04	2.80	2.80	4.76	3.32	3.00
MnO	0.04	0.07	0.06	0.06	0.11	0.06	0.08	0.06	0.07	0.21	0.07	0.08	0.05	0.05
MgO	1.48	1.20	1.69	1.28	2.82	1.61	1.25	1.61	0.72	2.61	2.22	4.98	4.44	4.60
CaO	2.45	3.36	2.35	2.31	0.99	2.90	3.37	0.36	2.50	1.40	1.06	1.25	1.19	1.02
Na^2O	4.63	4.70	4.23	4.23	5.87	4.35	4.18	6.01	4.18	3.49	6.02	5.97	7.48	8.08
K^2O	3.18	3.10	2.92	3.40	0.47	3.16	3.00	0.08	3.27	2.82	1.58	0.58	0.44	0.46
P^2O^5	0.17	0.15	0.18	0.15	0.13	0.20	0.17	N/D	0.19	0.19	0.18	0.19	0.17	0.17
LOI %	1.86	1.11	2.79	1.90	2.54	2.67	1.15	1.77	2.02	1.96	2.12	3.40	3.67	3.88
Total	99.59	99.91	99.56	99.81	99.76	99.72	98.96	98.52	99.85	99.88	99.74	99.54	99.55	99.64
PPM														
Ba	615	580	462	642	60	649	625	26	376	540	209	68	42	48
Sr	352	373	291	382	132	389	389	53	98	121	100	82	115	110
Nb	3.8	5.0	3.8	3.8	4.2	4.0	4.0	5.0	6.5	6.1	6.0	6.3	5.6	5.0
Hf	3.6	3.8	2.7	3.3	8.6	3.5	2.9	5.7	11.0	11.0	11.0	4.5	3.9	2.0
Zr	135	184	161	142	149	167	173	174	220	218	233	161	129	162
Y	11	12	12	13	13	14	12	25	27	24	24	23	24	21
Th	10.0	10.0	13.0	14.0	5.3	8.7	9.0	13.0	8.3	7.7	6.5	5.0	4.5	3.0
Cr	17	17	14	21	269	9	5	21	280	185	160	49	110	107
Co	6	8	9	6	7	6	7	6	7	9	14	17	21	25
Sc	5	4	5	5	9	—	—	9	15	13	12	17	22	17
V	49	47	65	58	56	54	50	41	102	109	71	58	133	138
Cu	28	6	36	11	81	150	13	10300	32	4	9	247	30	18
Zn	41	31	35	42	65	52	44	141	49	113	60	101	77	81
Ni	4	6	5	5	11	10	5	8	3	6	12	14	48	50
La	24	26	26	26	30	29	30	17	27	26	26	9	9	9
Ce	45	48	48	48	55	44	45	38	55	56	57	32	23	26
Nd	22	20	21	22	23	16	17	18	28	28	26	21	15	21
Sm	3.37	3.25	3.32	3.73	3.64	4.00	3.80	3.62	5.16	5.23	5.32	4.45	3.94	4.62
Eu	0.85	1.02	0.94	0.89	0.87	1.00	0.90	0.63	0.97	0.97	1.05	1.16	1.25	1.40
Gd	2.63	2.64	2.56	2.83	3.18	—	—	3.98	5.81	5.24	5.03	4.61	4.72	4.60
Dy	2.35	2.79	2.73	2.88	2.75	—	—	4.25	5.57	5.25	5.21	4.20	4.67	5.10
Ho	0.48	0.55	0.57	0.63	0.54	—	—	0.90	1.24	1.00	0.95	0.75	0.92	0.96
Er	1.36	1.45	1.69	1.78	1.44	—	—	2.45	3.03	2.41	2.70	1.84	2.20	2.23
Yb	1.41	1.41	1.70	1.80	1.43	1.30	1.30	2.46	3.27	2.37	2.66	1.80	2.24	2.17
Lu	0.22	0.22	0.25	0.27	0.21	0.22	0.22	0.41	0.50	0.35	0.40	0.27	0.34	0.33
TempZr (°C)	747	768	762	761	778	754	765	796	783	812	811	768	737	745

continued

Table 1 Continued

	Diorite porphyry				Polymictic breccia								
Sample	CPM-1.22	CPM-1.3	CPM-1.5	P-3-10	1301-250†	11,506-30†	11,497-278.5†	1301-158†	1301-200†	1301-202†	1301-240†	11,506-200†	11,506-330†
Wt %													
SiO^2	60.93	57.93	56.30	60.21	58.80	55.53	55.32	72.92	63.20	61.30	61.58	68.84	73.43
TiO^2	1.19	1.27	1.59	0.79	0.79	1.42	1.29	0.32	0.77	0.84	0.73	0.28	0.29
Al^2O^3	17.23	17.43	18.38	17.50	16.50	17.20	17.50	12.62	16.10	16.52	16.63	12.77	14.50
Fe^2O^3	1.89	2.59	2.87	3.55	1.55	3.46	2.88	1.27	1.50	1.48	1.40	2.77	0.10
FeO	2.56	3.56	3.20	1.68	3.88	4.80	5.04	1.20	2.80	3.48	4.00	2.80	1.96
MnO	0.03	0.07	0.11	0.10	0.20	0.08	0.11	0.06	0.11	0.16	0.26	0.03	0.04
MgO	2.19	3.28	4.14	3.47	5.04	4.80	4.24	1.13	2.62	3.70	3.32	1.05	0.89
CaO	0.76	0.90	1.25	0.92	2.33	1.73	2.50	1.87	2.29	1.82	1.38	0.60	0.60
Na^2O	8.57	8.04	7.11	8.39	6.56	3.96	6.55	6.30	7.00	7.25	6.25	3.05	4.17
K^2O	0.31	0.41	0.96	0.07	1.17	2.15	0.47	0.05	0.10	0.08	0.89	3.26	2.25
P^2O^5	N/D	N/D	0.21	0.21	0.17	0.24	0.21	0.09	0.22	0.25	0.19	—	0.08
LOI %	2.57	3.22	3.66	2.94	2.96	4.46	3.56	1.86	3.06	2.97	2.99	2.33	1.52
Total	98.23	98.70	99.78	99.83	99.95	99.83	99.67	99.69	99.77	99.85	99.62	97.78	99.83
PPM													
Ba	45	55	93	<5	87	213	50	23	21	29	77	513	331
Sr	110	107	130	97	142	110	78	43	163	131	200	56	121
Nb	5.6	5.0	5.0	4.0	3.6	4.0	3.9	4.2	5.0	4.1	3.8	4.1	4.2
Hf	5.2	2.2	4.0	2.3	3.6	5.1	5.1	16.0	5.5	5.1	3.8	15.0	16.0
Zr	199	149	175	132	123	168	191	155	196	163	143	140	155
Y	27	18	26	16	14	21	22	21	20	17	14	19	16
Th	4.8	3.0	5.2	<2	5.9	5.3	5.9	5.9	7.7	7.1	5.9	6.5	5.9
Cr	71	90	73	31	140	169	137	296	256	102	68	312	357
Co	16	18	21	11	17	23	23	7	10	17	18	3	2
Sc	17	17	21	11	15	22	20	6	13	14	12	4	4
V	109	123	133	82	142	165	152	53	95	100	108	21	24
Cu	14000	8500	192	67	6	500	16	580	109	46	39	21000	23
Zn	72	84	81	68	110	73	100	36	61	69	98	122	28
Ni	39	39	20	13	33	38	47	16	11	18	18	3	5
La	7	9	14	13	16	15	15	5	18	14	12	12	17
Ce	24	22	35	29	35	35	38	17	39	31	30	32	42
Nd	17	14	23	15	17	21	24	12	17	16	16	21	21
Sm	3.93	3.33	4.49	3.32	3.34	4.46	5.40	3.20	3.64	3.57	3.20	4.98	3.65
Eu	1.19	0.95	1.24	0.95	1.11	1.29	1.46	0.61	0.99	0.96	0.92	0.86	0.67
Gd	4.56	3.81	4.73	3.17	3.41	4.94	5.32	3.71	4.04	3.69	3.09	4.48	3.31
Dy	5.06	3.89	4.85	3.34	3.10	4.77	5.33	3.70	3.93	3.43	3.07	4.40	3.57
Ho	1.00	0.70	0.91	0.67	0.62	0.86	0.98	0.76	0.83	0.69	0.56	0.81	0.74
Er	2.45	1.70	2.31	1.59	1.46	2.27	2.46	1.84	2.10	1.65	1.47	2.01	1.94
Yb	2.40	1.70	2.25	1.57	1.36	2.27	2.37	1.83	2.09	1.59	1.45	1.95	1.92
Lu	0.37	0.25	0.37	0.22	0.21	0.35	0.36	0.27	0.31	0.23	0.21	0.29	0.31
Temp Zr (°C)	770	742	757	736	714	771	750	756	762	750	755	784	804

continued

Table 1 Continued

	Polymictic Breccia		Mafic dikes							
Sample	MB6‡	P-4-1	CPM-1.10	CPM-1.25	CPM-1.26	CPM-1.27	P-2-5	P-2-7	P-2-8	P-2-9
Wt %										
SiO^2	67.94	71.98	52.52	48.09	51.20	53.28	51.63	53.90	52.35	52.59
TiO^2	0.18	1.19	0.94	0.85	0.71	0.53	0.98	1.01	1.19	1.19
Al^2O^3	12.61	12.16	18.22	16.82	18.21	18.44	18.33	17.68	19.18	18.74
Fe^2O^3	6.65	1.11	3.63	4.05	2.82	4.15	4.46	3.68	4.98	3.89
FeO	—	4.04	3.92	4.20	4.60	2.40	2.76	4.20	3.72	4.72
MnO	0.08	0.09	0.16	0.19	0.10	0.10	0.11	0.15	0.21	0.22
MgO	2.64	2.11	4.92	7.27	3.94	3.81	5.09	3.55	2.78	3.29
CaO	0.27	0.04	4.98	6.64	4.18	8.04	5.57	6.43	7.80	6.14
Na^2O	2.70	5.48	3.88	4.23	5.44	3.98	3.57	3.71	3.61	3.78
K^2O	2.84	0.08	2.65	1.88	2.25	1.99	3.75	2.26	1.75	2.55
P^2O^5	0.06	—	0.15	0.14	0.16	0.17	0.11	0.35	0.43	0.44
LOI %	2.71	2.41	3.72	5.30	5.95	2.64	3.40	2.71	1.76	2.26
Total	98.69	99.69	99.69	99.66	99.56	99.53	99.76	99.63	99.76	99.81
PPM										
Ba	455	8	442	680	380	320	322	421	401	492
Sr	57	54	433	290	550	471	463	445	503	436
Nb	5.0	8.0	2.5	3.8	3.1	2.5	4.0	4.0	4.0	6.0
Hf	3.2	3.4	2.7	0.2	2.0	1.9	1.8	4.6	4.9	5.2
Zr	117	101	87	61	88	100	77	149	151	154
Y	16	17	16	14	16	10	17	23	28	27
Th	8.7	11.0	3.0	2.5	<2	3.0	<2	6.5	7.0	6.7
Cr	<1	9	43	269	25	76	45	16	9	9
Co	22	5	26	21	18	12	24	20	20	19
Sc	—	6	22	19	15	15	25	23	23	21
V	18	27	204	180	146	178	196	217	218	204
Cu	5640	2100	47	81	2	76	11	155	220	225
Zn	101	90	88	165	62	60	90	90	210	110
Ni	22	7	21	89	8	21	15	8	4	10
La	2	5	12	8	9	14	8	18	23	22
Ce	4	13	27	18	23	29	20	48	56	58
Nd	<5	8	17	15	17	16	13	28	32	32
Sm	2.00	2.21	3.56	2.89	3.42	3.04	3.07	5.33	7.09	6.98
Eu	0.30	0.29	1.19	0.99	1.07	1.04	1.19	1.38	1.72	1.70
Gd	—	2.78	3.63	2.84	3.06	2.56	3.54	5.27	6.49	6.00
Dy	—	3.39	3.12	3.38	3.25	2.35	3.43	4.87	5.71	5.81
Ho	—	0.71	0.66	0.71	0.62	0.47	0.65	0.86	1.10	1.12
Er	—	1.94	1.64	1.80	1.65	1.26	1.75	2.41	2.90	2.95
Yb	1.70	1.98	1.66	1.78	1.55	1.20	1.69	2.38	2.95	2.94
Lu	0.28	0.30	0.25	0.25	0.23	0.18	0.26	0.38	0.42	0.43
TempZr (°C)	780	757	668	585	644	652	647	699	702	710

Most samples are from open pit walls, except GP I samples, which were taken from a few km to the west and southwest of the pit.
†Samples from drill cores.
‡samples reported by Wittenbrink (2006).
<, below limit of detection; —, not analyzed; GP, granodiorite phorphyry; LOI, loss on ignition; TempZr, zircon saturation temperature.

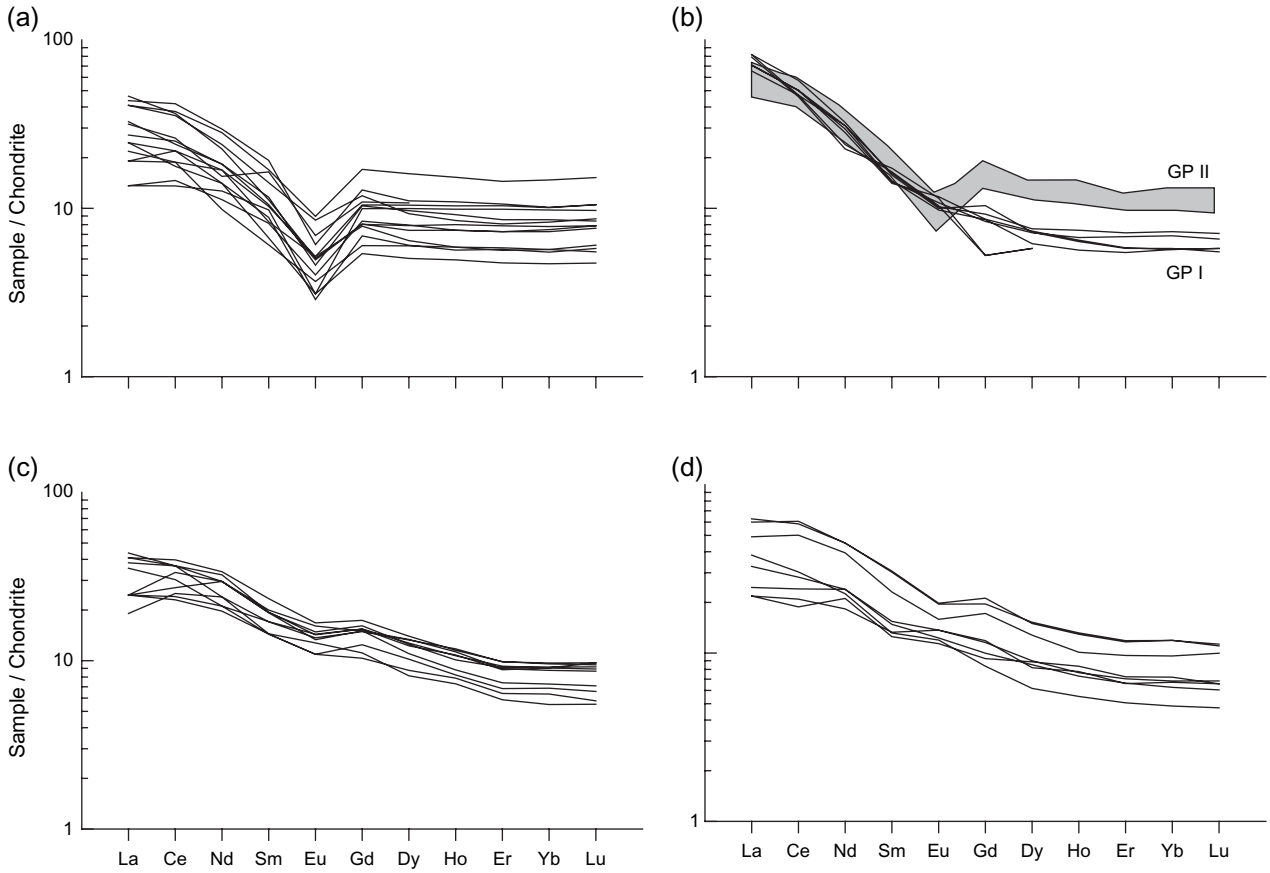

Fig. 5 Chondrite-normalized rare earth element patterns of rock samples from Mantos Blancos. (a) Rhyolite dome; (b) granodiorite phorphyry; (c) diorite porphyry; (d) mafic dike.

6. Silicate melt inclusions hosted in quartz

Silicate MI hosted in quartz phenocrysts of the GP II, and quartz crystals of the polymictic breccia were analyzed using a Cameca SX 100 electron microprobe (TU Clausthal, Zellerfeld, Germany). An accelerating voltage of 15 kV, beam current of 8 nA, beam diameter of 3 μm and a counting time of 6 s were chosen for major elements, and 20 kV, beam current of 40 nA, and a counting time of 20 s for trace elements.

The sample preparation by remelting can introduce contamination by silica from the host quartz. Webster *et al.* (2004) discussed in detail the difficulties in determining appropriate heating times and temperatures for remelting of MI characterized by variable compositions. Based on the empirical results obtained in the laboratory, the best conditions for the experiments in quartz are 950°C and 101.325×10^3 Pa external pressure during 24 h (Dietrich, 1999; Wittenbrink, 2006). After the heating experiments, the samples were quenched to produce a silicate glass. The homogenized MI are small (15–40 μm), in some cases with a vapor bubble (1–10 μm) of 5–15% in volume relative to the MI. Although the heating temperature (950°C) seems to be high, after 24 h (only in very small inclusions <10 μm) the host quartz walls were partially melted, and few larger inclusions were not entirely re-homogenized.

The MI were located towards the central portions of their host embayed β-quartz crystals, phenocrysts formed early in the crystallization of Mantos Blancos acidic magmas. At least three individual analyses were carried out on each MI, hence the reported values in Table 3 are averages of several analytical spots. The analytical data of MI, within each lithological unit, have relatively low dispersion in silica content, and average data were used for major elements (Table 3, Fig. 7). In general the SiO_2 concentrations of the MI

Table 2 Sr-Nd isotope data from Mantos Blancos ore deposit

Sample	Rock unit	Rb (ppm)	2σ	Sr (ppm)	2σ	$^{87}Sr/^{86}Sr$	2σ	$^{87}Rb/^{86}Sr$	2σ	$(^{87}Sr/^{86}Sr)_o$
MB1†	Rhyolitic dome	3.155	0.032	37.68	0.30	0.7065	0.00001	0.242	0.004	0.7059
MB6	Polymictic breccia	119.4	1,660	55.21	0.57	0.7184	0.00002	6.264	0.081	0.7059
MB3	GP I	81.19	0,810	391.55	3.13	0.7051	0.00001	0.600	0.008	0.7039
MB4	GP I	79.98	0,800	382.43	3.06	0.7048	0.00001	0.605	0.008	0.7036
MB-sp-7	Diorite porphyry	52		88		0.71452		4.94		0.704549
MB-sp-46	Diorite porphyry	71		100		0.71374		4.04		0.705586
MB-sp-60	Diorite porphyry	120		101		0.71061		2.42		0.705725

Sample	Rock unit	Sm (ppm)	2σ	Nd (ppm)	2σ	$^{143}Nd/^{144}Nd$	2σ	$^{147}Sm/^{144}Nd$	2σ	$(^{143}Nd/^{144}Nd)_o$	Nd
MB1†	Rhyolitic dome	4.236	0.004	16.511	0.02	0.51249	0.000006	0.1551	0.0008	0.51234	–2.0
MB6	Polymictic breccia	1.211	0.001	3.352	0.004	0.51267	0.000008	0.2184	0.0011	0.51247	0.1
MB3	GP I	4.29	0.004	24.32	0.031	0.51272	0.000008	0.1067	0.0005	0.51263	3.2
MB4	GP I	4.351	0.004	23.199	0.03	0.51274	0.000007	0.1134	0.0006	0.51264	3.5
MB-sp-7	Diorite porphyry	2		6.56		0.512646		0.1620		0.512498	0.77
MB-sp-46	Diorite porphyry	5.64		24.82		0.512694		0.1208		0.512583	2.45
MB-sp-60	Diorite porphyry	5.49		23.73		0.512569		0.1230		0.512456	–0.03

All samples were obtained from the open pit walls, except samples from the GP I unit, located a few km to the west and southwest of the pit. The samples MB-sp-7, MB-sp-46 and MB-sp-60 correspond to diorite porphyry unit from the pit (F. Munizaga, pers. comm., 2006). All samples were recalculated to 142 Ma, except † recalculated to 155 Ma.
GP, granodiorite phorphyry.

trapped in quartz phenocrysts of the rhyolitic dome (Wittenbrink, 2006) resemble the bulk rock composition. In contrast, the MI from the GP II and the polymictic breccia have higher SiO_2 contents than their host rocks. An intriguing feature of the MI is their copper concentrations. Extremely high copper contents have been detected in MI from the rhyolitic dome (323–13400 ppm; Wittenbrink, 2006). Cu contents between 60 and 1665 ppm have been measured in the GP II, whereas low Cu contents (55–150 ppm) have been obtained in MI from the polymictic breccia.

7. Discussion

7.1. Origin of the rhyolitic melts

The high-silica rhyolite composition of the dome represents an oddity within the large volume of mafic–intermediate Jurassic magmatism of the coastal range, which is strongly dominated by mantle-derived andesitic and basaltic volcanic rocks of the La Negra Formation. The enriched Sr-Nd isotopic signatures of the rhyolitic dome are consistent with a provenance from a crust-dominated source. A crustal melt, with a near-thermal-minimum composition like that of the rhyolitic dome, should have consistent near-solidus temperature of formation. To estimate the maximum temperature of the rhyolite dome we use zircon saturation thermometry (Watson & Harrison, 1983; Miller *et al.*, 2003). Zircon saturation temperatures (T_{Zr}), calculated from bulk rock compositions, provide maximum estimates of temperature if the magma is oversaturated in zircon. Because solubility of zircon is sensitive to temperature but insensitive to pressure, the zircon saturation temperature allows inference of the magma temperature at the source if the magma has abundant inherited zircon (oversaturated). A temperature of approximately 750°C (Fig. 8) has been obtained for the rhyolitic dome. At this temperature a rhyolitic melt is unlikely to have resulted from significant crystal fractionation

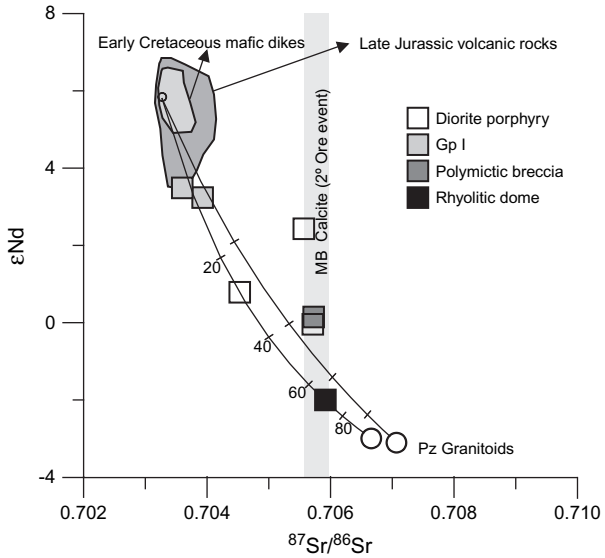

Fig. 6 εNd and $^{87}Sr/^{86}Sr_i$ isotope data from Mantos Blancos, with reference data from Late Jurassic volcanic rocks of the La Negra Formation, Cretaceous dikes of the Coastal Range (Rogers & Hawkesworth, 1989; Lucassen *et al.*, 2002) and Paleozoic granitoids (Lucassen *et al.*, 1999). Lines with tick marks represent a simple mixing model. The grey vertical field represents the $^{87}Sr/^{86}Sr$ ratio of calcites from the propylitic assemblage of Mantos Blancos (Tassinari *et al.*, 1993). All isotope data are recalculated to age of emplacement and Paleozoic granitoids to 150 Ma.

of a more mafic (and high temperature) parental melt. Moreover, considering that hornblende fractionation has been invoked as an efficient mechanism to yield felsic magmas from a basic–intermediate parental liquid, the REE patterns of the rhyolitic dome (Fig. 5) preclude hornblende participation in the magma fractionation. It is likely, therefore, that the rhyolites formed by partial melting of quartz–feldspathic rocks of crustal origin. Advanced fractionation of a more primitive parental magma or partial melting of mafic source material equilibrated under lower crust (garnet–amphibolite facies) conditions is less likely. The compositional similarities among the rhyolitic dome and the MI in quartz, regardless of the host rock, may indicate that both represent evolved magmas generated through similar processes. Therefore, the crustal signature in the Sr-Nd isotopic composition and in the REE patterns of the rhyolitic dome can be inherited by the MI.

The coeval development of mafic magmatism and felsic magmatism in the Mantos Blancos ore deposit suggests a cause-and-effect relationship, in which the heat source for the generation of the rhyolite melts would be the mafic magma injected into the felsic crust. In this scenario the participation of two contrasting magma sources (crust and mantle) could be highly variable and deserves to be assessed. Simple mixing models (Faure, 1986) are shown in Figure 6 in order to test the degree of involvement of felsic crust and mantle in the Sr-Nd isotopic signatures of the rhyolitic magmas. The boundary conditions for the modeling are defined by the starting compositions, which are represented by the average composition of the mantle-derived mafic volcanic rocks of the La Negra Formation (Rogers & Hawkesworth, 1989; Lucassen *et al.*, 2002) and by the composition of the felsic Paleozoic granitoids of the Coastal Range near Mantos Blancos (Lucassen *et al.*, 1999). Despite the wide range of the calculated crust/mantle ratios in the source (Fig. 7), a crustal-dominated source can best explain the isotopic signatures of the rhyolitic magmas.

7.2. Origin of the intermediate rocks (GP I and GP II): Crystal fractionation and magma mixing

The REE patterns indicate two distinct fractionation paths for the Mantos Blancos intermediate rocks. The concave shape of the HREE distribution, and the absent or subtle negative Eu anomalies in mafic dikes, diorites and GP I, suggest hornblende-dominated fractionation for this magmatic suite, which in turn is consistent with the hornblende fractionation vector shown in Figure 9. These data suggest a GP I derivation from a dioritic parental magma. In contrast, the negative Eu anomalies in the GP II suggest plagioclase-dominated fractionation, probably at low oxygen fugacity. But the distribution of GP II samples in Figure 9 differs from the plagioclase fractionation vector, suggesting an overprinting of magma mixing effects. In fact, shallow magma interaction explains both the GP II formation by magma mixing (Fig. 3g, h) and the polymictic breccia by magma mingling. The invariably rhyolitic composition of the MI in quartz phenocrysts, regardless of the composition of the host rock, would represent the felsic end-member composition of the mixing, whereas the dioritic porphyry would represent the mafic end-member composition. This hypothesis is supported by (i) the presence of abundant mingled fragments of mafic (dioritic porphyry) and felsic (granodioritic porphyries) rocks observed in polymictic magmatic breccia drill core samples (Fig. 3g, h); and (ii) the commonly observed disequilibrium textures in the GP II, such as

Table 3 Melt inclusions analyses from Mantos Blancos ore deposit. Major elements in wt %, Cu in ppm

Sample	Polymictic breccia					GP II				
	506a-3	506a-5	506a-2d	Average	SD	497-5b	497-3b	497-2b	Average	SD
Wt%										
SiO^2	72.69	73.00	74.26	73.32	0.83	72.67	72.76	75.25	74.89	1.98
TiO^2	0.07	0.01	0.09	0.06	0.04	0.09	0.20	0.17	0.15	0.06
Al^2O^3	14.26	16.79	13.33	14.80	1.79	12.04	12.07	11.48	11.86	0.33
FeO	1.43	0.17	0.73	0.77	0.63	0.74	2.41	1.85	1.67	0.85
MnO	0.09	0.01	0.04	0.05	0.04	0.01	0.03	0.06	0.04	0.02
MgO	0.51	0.00	0.10	0.21	0.27	0.06	0.87	0.33	0.42	0.41
CaO	2.45	0.47	0.97	1.29	1.03	0.41	1.01	0.45	0.62	0.33
Na^2O	3.89	2.11	3.40	3.13	0.92	3.50	2.12	2.89	2.84	0.69
K^2O	3.03	3.94	2.52	3.16	0.72	3.86	0.08	1.84	1.93	1.90
Total	98.53	96.55	95.49	96.86	1.54	97.49	91.71	94.77	94.66	2.89
Cu ppm	150	55	67	91	52	60	ND	1665	863	1135

Sample	Rhyolitic dome									
	MB5-1 × 3a	MB5-3 × 1a	MB5-3 × 2a	MB5-3 × 8a	MB5-3 × 10a	MB5-2 × 15a	MB5-2 × 15a	MB5-3 × 3a	Average	SD
Wt%										
SiO^2	69.17	73.95	74.94	71.39	77.58	71.77	72.73	72.40	72.99	2.53
TiO^2	0.14	0.02	0.13	0.16	0.12	0.04	0.09	0.27	0.12	0.08
$Al2O^3$	14.07	14.12	14.95	16.29	11.81	16.68	21.88	9.48	14.91	3.67
FeO	2.59	0.45	1.13	1.12	1.01	0.88	0.39	2.79	1.29	0.91
MnO	0.03	0.02	0.02	0.02	0.01	0.01	0.02	0.07	0.02	0.02
MgO	0.35	0.02	0.08	0.05	0.03	0.19	0.16	0.46	0.17	0.16
CaO	0.48	0.48	0.61	0.55	0.39	0.46	0.02	0.16	0.39	0.20
Na^2O	2.53	3.97	3.09	3.97	3.07	6.22	1.18	3.29	3.41	1.44
K^2O	5.35	3.65	4.19	4.39	2.72	4.39	1.00	1.55	3.41	1.52
P^2O^5	0.03	0.06	ND	0.03	0.03	0.02	0.05	0.05	0.04	0.02
Total	94.68	96.73	99.24	98.01	96.71	100.70	97.80	90.69	96.82	3.06
Cu ppm	10530	1787	323	373	1170	5783	ND	13367	4762	5308

Melt inclusions from polymictic breccia came from sample 11506–200 and GP II melt inclusions from sample 11497–320. Melt inclusions from rhyolitic dome were obtained from sample MB5, reported by Wittenbrink (2006).
GP, granodiorite phorphyry; ND, not detected.

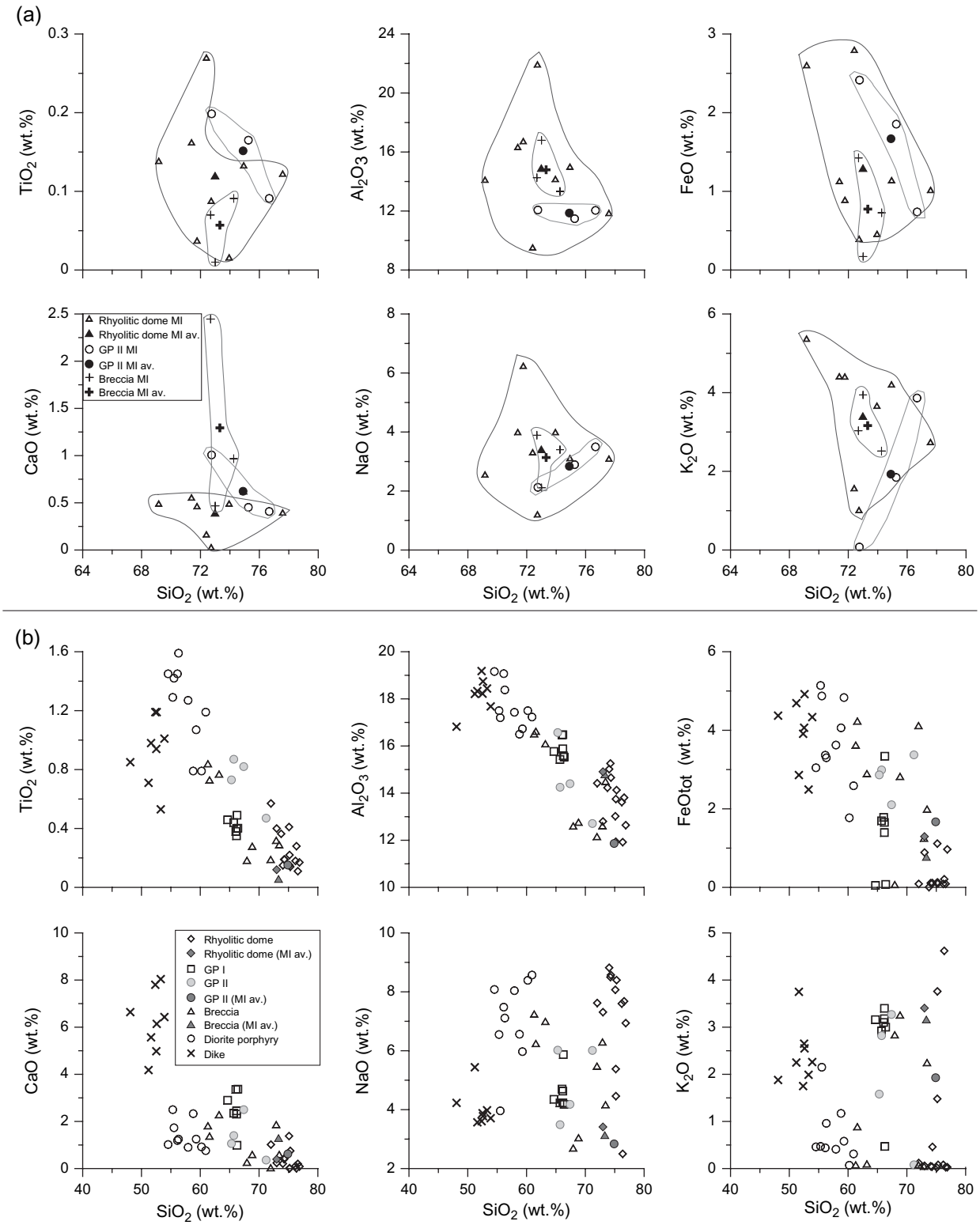

Fig. 7 Selected major element variation diagrams of (a) melt inclusions and (b) whole rock analyses of Mantos Blancos rocks. The average of melt inclusions data is also plotted for comparison with their host rocks.

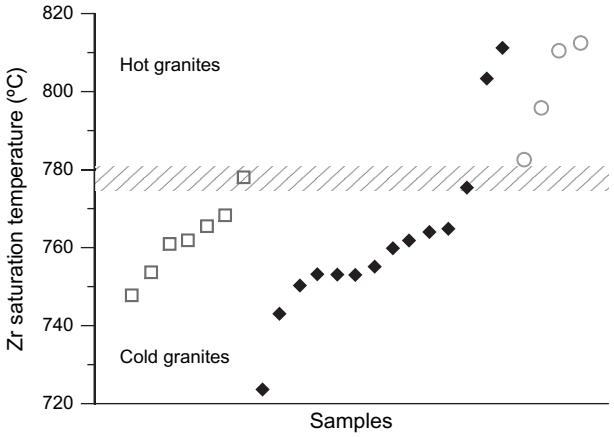

Fig. 8 Zircon saturation temperature (T_{Zr}) of felsic-intermediate rocks in the Mantos Blancos district. The shaded area represents the transition of cold and hot granites of Miller *et al.* (2003). (□) granodiorite porphyry I (GP I); (○) GP II; (♦) Rhyolitic dome.

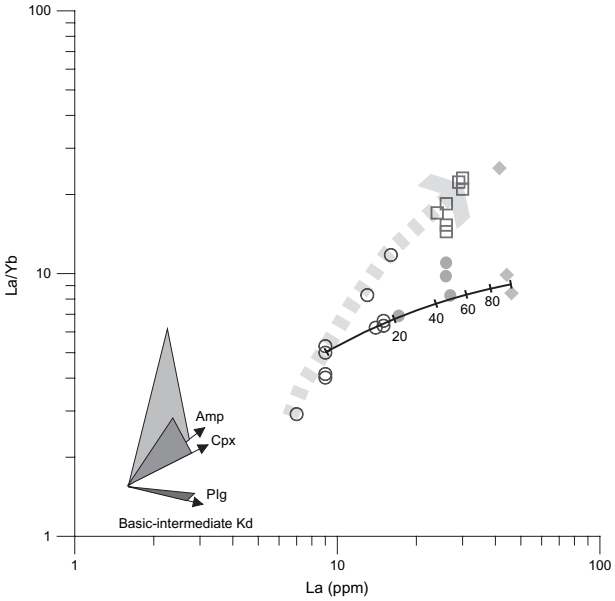

Fig. 9 La vs La/Yb diagram. The data define two trends: one dominated by hornblende fractionation (dashed grey line) and the other dominated by magma mixing (solid line with tick marks) over imposed to plagioclase fractionation. Because no REE data are available from GP II melt inclusions, we chose melt inclusion data from the rhyolitic dome (Wittenbrink, 2006) as end-member of the mixing model. The mafic end-member corresponds to the average of the diorite samples. Rayleigh fractionation vectors of different minerals are shown according to crystal-melt partitioning data for basic and intermediate magma by Keskin (2002). The size of the vectors is equal to 50% of crystallization. Note that small vertical apparent trend does not constitute necessarily an evolution trend. (□) granodiorite porphyry I (GP I); (●) GP II; (○) diorite; (◆) rhyolitic dome melt inclusion.

corroded quartz phenocrysts (Fig 3f). Although the disequilibrium textures can be explained by mechanisms of decreasing pressure and/or increasing temperature in the magma chamber, we prefer the second alternative because the GP II exhibits the highest T_{Zr} (780–810°C; Fig. 8), consistent with a thermal input derived from the diorite intrusion into the felsic magma system. A scheme of the petrogenetic model for the Mantos Blancos system is given in Figure 10. It consists of two magmatic suites with distinct origin: a mantle-dominated suite represented by diorites, mafic dikes and GP I, and a crustal-dominated suite represented by the rhyolitic magmas. Magmas from the two suites interacted to give rise to GP II and polymictic magmatic breccias.

7.3. Metallogenic considerations

Considering that (i) the Jurassic–early Cretaceous magmatism in the Coastal Range of northern Chile is characterized by mantle-dominated volcanism (Rogers & Hawkesworth, 1989; Lucassen *et al.*, 2002); (ii) the volume of high-silica rocks (like the rhyolitic dome), of probably crustal-dominated source, is very restricted in a regional scale; and (iii) the mineralization in numerous copper deposits (including Mantos Blancos) hosted in Jurassic volcanic rocks of the Coastal Range, is coeval with stocks and sills of mainly dioritic composition, and are intruded by post-mineralization basaltic dikes (Maksaev & Zentilli, 2002), the hydrothermal fluids and associated mineralization in the Mantos Blancos system were probably derived from mafic–intermediate magmas such as the basaltic dikes and diorites. Basaltic dikes have also been described in the Bingham porphyry copper, where they have been considered as the potential metal source for the mineralization (Keith *et al.*, 1997). A similar case has been described by Halter *et al.* (2005) in Bajo La Alumbrera Cu-Au porphyry. In these two deposits the ore is hosted by more felsic rocks (Halter *et al.*, 2005).

In the Mantos Blancos Cu deposit the second magmatic hydrothermal event was temporally and spatially associated with the dioritic and granodioritic porphyry emplacement, and thus is consistent with a magma mingling process. In this scenario the intrusion of porphyry diorite magma within a colder and shallow rhyolitic magma chamber could supply not only heat

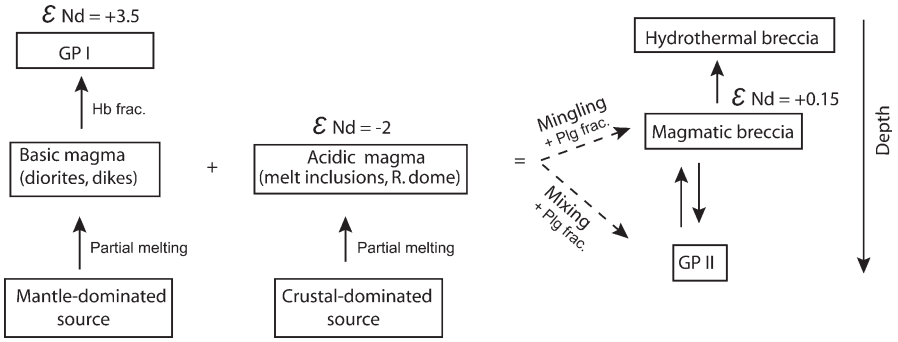

Fig. 10 Schematic diagram of the Mantos Blancos petrogenetic model.

and volatiles during quenching but also metals. The magma mingling processes may have induced the early release of copper-bearing fluids from the quenched mafic hydrous magma, contributing to the mineralization in the polymictic magmatic hydrothermal breccias, porphyries and rhyolitic dome of the Mantos Blancos deposit. Although the proportion of felsic/mafic magma in the interaction process is unknown, the mixing line of Figure 9 suggests a larger volume of felsic magma, which is consistent with the quartz phenocrysts preservation in it.

The slightly radiogenic Sr initial ratios of altered rocks in Mantos Blancos (Fig. 6) resemble those obtained in hydrothermal calcites of the deposit (Tassinari *et al.*, 1993). According with Tassinari *et al.* (1993), this high Sr initial ratio suggests that hydrothermal fluids were not entirely magmatic and/or that isotopic equilibrium between host rocks and the ore-bearing hydrothermal fluids occurred.

8. Conclusions

In the Mantos Blancos copper deposit the emplacement of dioritic and granodioritic porphyry during the early Cretaceous was related to the major hypogene copper sulfide mineralization. Two different trends of magma evolution were recognized in these rocks, which resulted in two types of granodioritic porphyry: GP I and GP II. The first trend is represented by mafic dikes, dioritic and GP I porphyries, that evolved by hornblende-dominated fractionation, from a mantle-dominated source. The second trend is represented by dioritic porphyries and GP II. Low-pressure mixing and mingling of dioritic magmas and rhyolitic melts of crustal origin are likely for the formation of GP II and polymictic breccias, respectively. The MI analyzed in quartz from GP II and in the polymictic magmatic hydrothermal breccia of the deposit are compositionally more evolved than their host rocks, reinforcing the hypothesis of magma interaction as a genetic mechanism. Field, geochemical and petrographic data in Mantos Blancos deposit point to an interaction between dioritic and siliceous magmas. This interaction may cause the release of hydrothermal fluids from the higher temperature component, during quenching.

Acknowledgments

This study was funded by FONDEF (CONICYT, Chile), grant DO1-1012, assigned to the authors and to the Mantos Blancos division of Anglo American Chile. Permission for publication was established between the University of Chile, the Chilean Government and the Company grant-related contract. Thanks to the geologists of the Mantos Blancos mine with whom we had the pleasure to work. Special acknowledgment to J. Martinez and J. Schneider who carried out geochemical and isotopic analyses, respectively, and to K. Herrmann for help with the EMPA data acquisition. The first author benefited from the MECESUP program of the Chilean Government to support PhD studies. Special thanks to Bernd Lehmann, Alcides Sial and Francisco Munizaga for helpful comments that greatly improved the manuscript. The manuscript was largely improved by comments and suggestions of W. Halter and I. Miyagi, as well as from the careful editorial handling.

References

Andriessen, P. A. and Reutter, K.-J. (1994) K-Ar and fission track mineral age determination of igneous rocks related to multiple magmatic arc systems along the 23°S latitude of Chile and

NW Argentina. *In* Reutter, K.-J., Scheuber, E. and Wigger, P. J. (eds.) Tectonics of the Southern Central Andes. Structure and evolution of an active continental margin. Springer Verlag, Stuttgart, 141–153.

Birck, J. L. (1986) Precision K-Rb-Sr isotopic analyses: Application to Rb-Sr chronology. Chem. Geol., 56, 73–83.

Camus, F. (2003) Geología de los sistemas porfíricos en los Andes de Chile. Sernageomin, Chile, 267p.

Chávez, W. (1985) Geological setting and the nature and distribution of disseminated copper mineralization of the Mantos Blancos district, Antofagasta Province, Chile (PhD Thesis). University at California, Berkeley, CA, USA.

Dallmeyer, R. D., Brown, M., Grocott, J., Taylor, G. K. and Treolar, P. J. (1996) Mesozoic magmatic and tectonic events within the Andean plate boundary zone, 26°–27°30′S, North Chile: Constraints from $^{40}Ar/^{39}Ar$ mineral ages. J. Geol., 104, 19–40.

Dietrich, A. (1999) Metallogenie, Geochemie und Schmelzeinschluss-Untersuchungen von tin porphyry und copper porphyry Lagerstätten in den zentralen Anden (Bolivien, Chile) (PhD Thesis). Clausthal University of Technology, Clausthal-Zellerfeld, Germany.

Espinoza, S., Véliz, H., Esquivel, J., Arias, J. and Moraga, A. (1996) The cupriferous province of the Coastal Range, Northern Chile. *In* Camus, F., Sillitoe, R. H. and Petersen, R. (eds.) Andean copper deposits: New discoveries, mineralization, styles and metallogeny. Soc. Econ. Geol. Special Publ. 5, 19–32.

Faure, G. (1986) Principles of isotope geology, 2nd edn. John Wiley & Sons, New York, 589p.

Floyd, P. A. and Winchester, J. A. (1978) Identification and discrimination of altered and metamorphosed volcanic rocks using immobile elements. Chem. Geol., 21, 291–306.

Halter, W. E., Heinrich, C. A. and Pettke, T. (2005) Magma evolution and the formation of porphyry Cu-Au ore fluids: Evidence from silicate and sulfide melt inclusions. Mineral. Deposita, 39, 845–863.

Keith, J. D., Whitney, J. A., Hattori, K., Ballantyne, G. H., Christiansen, E. H., Barr, D. L., Cannan, T. M. and Hooks, C. J. (1997) The role of magmatic sulphides and mafic alkaline magmas in the Bingham and Tintic mining districts, Utah. J. Petrol., 38, 1679–1690.

Keskin, M. (2002) FC-Modeler: A Microsoft® Excel© spreadsheet program for modeling Rayleigh fractionation vectors in closed magmatic systems. Comput. Geosci., 28, 919–928.

Kramer, W., Siebel, W., Romer, R. L., Haase, G., Zimmer, M. and Ehrlichmann, R. (2005) Geochemical and isotopic characteristics and evolution of the Jurassic volcanic arc between Arica (18°30′S) and Tocopilla (22°S), North Chilean Coastal Range. Chem. Erde Geochem., 65, 47–78.

Lucassen, F., Franz, G., Thirlwall, M. F. and Mezger, K. (1999) Crustal recycling of metamorphic basement: Late Paleozoic granites of the Chilean coast range and precordillera at –22°S. J. Petrol., 40, 1527–1551.

Lucassen, F., Escayola, M., Romer, R. L., Viramonte, J., Koch, K. and Franz, G. (2002) Isotopic composition of Late Mesozoic basic and ultrabasic rocks from the Andes (23–32°S): Implications for the Andean mantle. Contrib. Mineral Petrol., 143, 336–349.

Maksaev, V. and Zentilli, M. (2002) Chilean stratabound Cu-(Ag) deposits: An overview. *In* Porter, T. M. (ed.) Hydrothermal iron oxide copper–gold and related deposits: A global perspective, 2. PCG Publishing, Adelaide, Australia, 185–205.

Miller, C. F., McDowell, S. M. and Mapes, R. W. (2003) Hot and cold granites?: Implications of zircon saturation temperatures and preservation of inheritance. Geology, 31, 529–532.

Oliveros, V. (2005) Les formations magmatiques jurassiques et mineralisation du nord Chili, origine, mise en place, alteration, metamorphisme: etude geochronologique et geochemie (PhD Thesis). Universite de Nice-Sophia Antipolis, France.

Palacios, C. (1984) Considerations about the plate tectonic models, volcanism, and continental crust in the Southern part of the Central Andes. Tectonophysics, 108, 205–214.

Perelló, J., Martini, R., Arcos, R. and Muhr, R. (2003) Buey Muerto: Porphyry copper mineralization in the early Cretaceous arc of northern Chile. *In* Proceeding 10th Congreso Geológico de Chile. Concepción, Chile. (Electronic version).

Pichowiak, S. (1994) Early Jurassic to Early Cretaceous magmatism in the Coastal Cordillera and the Central depression of North Chile. *In* Reutter, K.-J., Scheuber, E. and Wigger, P. J. (eds.) Tectonics of the Southern Central Andes. Structure and evolution of an continental margin. Springer Verlag, Stuttgart, 203–217.

Pichowiak, S., Buchelt, M. and Damm, K. W. (1990) Magmatic activity and tectonic setting of early stages of Andean cycle in northern Chile. Geol. Soc. Am. Special Paper 241, 127–144.

Pin, C. and Zalduegui, J. F. S. (1997) Sequential separation of light rare-earth elements, thorium and uranium by miniaturized extraction chromatography: Application to isotopic analyses of silicate rocks. Anal. Chim. Acta, 339, 79–89.

Ramírez, L. E., Palacios, C., Townley, B., Parada, M. A., Sial, A. N., Fernandez-Turiel, J. L., Gimeno, D., Garcia-Valles, M. and Lehmann, B. (2006) The Mantos Blancos copper deposit: An Upper Jurassic breccia–style hydrothermal system in the Coastal Range of Northern Chile. Mineral. Deposita, 41, 246–258.

Rogers, G., Hawkesworth, C. J. (1989) A geochemical traverse across the North Chilean Andes: Evidence for crust generation from the mantle wedge. Earth Planet. Sci. Lett., 91, 271–285.

Scheuber, E. (1994). Tektonische Entwicklung des nordchilenischen aktiven Kontinentalrandes: Der Einfluss von Plattenkonvergenz und Rheologie. Geotekt. Forsch., 81, 1–131.

Scheuber, E. and Gonzalez, G. (1999) Tectonics of the Jurassic–Early Cretaceous magmatic arc of the North Chilean Coastal Cordillera (22°–26°S): A story of crustal deformation along a convergent plate boundary. Tectonics, 18, 895–910.

Tassinari, C., Munizaga, F. and Ramírez, R. (1993) Edad y geoquímica isotópica Rb-Sr del yacimiento de cobre Mantos Blancos: Relación temporal con el magmatismo jurásico. Rev. Geol. Chile, 20, 193–205.

Watson, E. B. and Harrison, T. M. (1983) Zircon saturation revisited: Temperature and composition effects in a variety of crustal magma types. Earth Planet. Sci. Lett., 64, 295–304.

Webster, J. D., Thomas, R., Förster, H. J., Seltmann, R. and Tappen, C. (2004) Geochemical evolution of halogen-enriched granite magmas and mineralizing fluids of the Zinnwald tin-tungsten mining district, Erzgebirge, Germany. Mineral. Deposita, 39, 452–472.

Wittenbrink, J. (2006) Geochemische, metallogenetische und Bor-Isotopen Untersuchungen an Schmelzeinschluessen und Gesteinen bolivianischer und chilenischer porphry-Lagerstätten der zentralen Anden (PhD Thesis). Clausthal University of Technology, Clausthal–Zellerfeld, Germany.

Appendix I

Analytical method of Sr-Nd isotopes

Powdered rock samples were weighed into clean Teflon screw-top beakers and spiked with mixed ^{87}Rb-^{84}Sr and ^{149}Sm-^{150}Nd tracers. The samples were completely dissolved in a 3:1 mixture of 22 N HF/14 N HNO_3 on a hotplate at approximately 110°C. All solutions were evaporated to dryness and redissolved in aqua regia, evaporated again and then rewetted with 2 N HNO_3. Rb, Sr, Sm and Nd were chemically separated using a tandem column elution scheme, modified from Pin and Zalduegui (1997). The sample solutions were transferred to preconditioned small-size (50 μL) Teflon columns containing Eichrom Sr Resin (Darien, IL, USA), coupled with a second set of 50 μL columns containing Eichrom Tru Resin (Eichrom Sr Resin, Darien, IL, USA) to adsorb the rare earth elements (REE). After collecting the Rb during the first elution step and further washing with 2 N HNO_3, Sr and REE were stripped from the decoupled columns with 1.3 mL of double deionized water (DDW). The REE cut was directly eluted onto 1 mL columns containing Eichrom Ln Resin (Eichrom Sr Resin, Darien, IL, USA) and washed with 9.5 mL of 0.25 N HCl. Nd was then eluted with 4 mL of 0.25 N HCl prior to elution of Sm with 2 mL of 0.75 HCl.

For mass spectrometry, Sr was loaded with $TaCl_5$-HF-H_3PO_4 solution (Birck, 1986) onto W single filaments, and Rb, Sm and Nd loaded with DDW onto the evaporation ribbon of double-Ta and double-Re filament assemblages, respectively. All isotopic measurements were performed on a six-collector Finnigan MAT 261 solid-source mass spectrometer (Finnigan MAT GmbH, Bremen, Germany) running in static multicollection mode. Sr isotopic ratios were normalized to $^{88}Sr/^{86}Sr = 0.1194$ and Nd isotopic ratios normalized to $^{146}Nd/^{144}Nd = 0.7219$. Repeated static measurements of the NBS 987 Sr isotope standard and the La Jolla Nd standard over the duration of the present study yielded $^{87}Sr/^{86}Sr = 0.71025 \pm 0.00004$ (2σ mean, $n = 12$) and $^{143}Nd/^{144}Nd = 0.511848 \pm 0.000009$ (2σ mean, $n = 8$). Maximum total procedure blanks ($n = 6$) amounted to 30 pg Sr, 5 pg Rb, and 50 pg Sm and Nd. They were found to be negligible with respect to the analyzed sample amounts.